Forward elastic recoil measurements using heavy ions

R. Siegele, H. K. Haugen,[a] and J. A. Davies
Accelerator Laboratory, McMaster University, Hamilton, Ontario L8S 4K1, Canada

J. S. Forster and H. R. Andrews
AECL Research, Chalk River Laboratories, Chalk River, Ontario K0J 1J0, Canada

(Received 2 May 1994; accepted for publication 5 July 1994)

The application of the elastic recoil detection technique utilizing heavy ions for the analysis of semiconductor samples is demonstrated. With this technique the depth profiles of the primary constituents as well as profiles of all impurities can be measured in one spectrum. Depending on the target material, a depth resolution down to 20 nm can be achieved. All elements except hydrogen can be detected with almost the same sensitivity, namely $\sim 1\times 10^{15}$ at/cm^2 with 136 MeV I in a 30° recoil geometry. For hydrogen, the sensitivity is about four times better.

I. INTRODUCTION

Different ion-beam techniques are used to measure atomic profiles in the surface region with high sensitivity. Rutherford backscattering analysis (RBS), using ^{4}He ions, is a powerful nondestructive tool to profile impurities in the surface region (~ 1 μm) of solids and it has become a standard technique in most accelerator laboratories. However, the use of RBS is limited because He projectiles backscattered from light surface atoms and heavier bulk atoms deeper in the sample have the same energy; therefore, the detection of light elements in a heavier matrix is often difficult, especially if only trace amounts are present. This is made even worse by the smaller Rutherford cross section of low-Z elements, compared to the cross section of the heavier and more abundant bulk atoms.

Low-Z elements such as hydrogen, carbon, nitrogen, and oxygen play a very important role in the processing of semiconductors, especially in chemical-vapor-deposited (CVD) or molecular-beam-epitaxy (MBE) grown films. Therefore, a way to measure these impurities and their depth distribution is very important. Different accelerator techniques such as nuclear reactions[1] and resonances[1,2] have been used to detect and profile some of these elements, but for each element a specific reaction or resonance is needed.

L'Ecuyer *et al.*[3,4] developed forward elastic recoil detection to measure low-Z surface impurities, such as H, D, Li, C, and O in a heavier substrate. They used a thin Mylar film to prevent the heavier bulk recoils and scattered projectiles from reaching the detector.

Since hydrogen is a very frequently encountered impurity, which is often difficult to measure with other techniques, forward elastic recoil detection analysis (ERDA) using a beam of He has been widely used for H profiling.[5] The energy spectrum of the ejected H atoms is measured with a surface barrier detector. The He projectiles as well as heavier recoil atoms are stopped in a Mylar foil, leaving only the energy spectrum of the H recoils.

Recently, the ERDA technique has been extended with special detectors, which allow the separation of different recoil species.[6–17] Since the detected particle is the recoil, different elements can be separated by either their nuclear charge or their mass. Time-of-flight (TOF) and gas detectors, such as a Bragg detector and various types of ΔE-E detectors, have been developed to achieve this separation. The depth profile of each elemental species may then be derived from its energy spectrum.

In order to detect also the heavy components of a target, their recoils have to be energetic enough to reach the surface and be detected. In the pure Coulomb regime, where the Rutherford scattering law applies, sufficiently high recoil energies can only be obtained with higher-energy, heavy projectiles. Heavy projectiles also improve the sensitivity because of their higher cross sections.

The first part of this article contains a theoretical evaluation of the sensitivity, depth, and species resolution for different experimental setups. In the second part, the advantages of high-Z, high-E beams are demonstrated with typical samples produced in many laboratories involved in device fabrication. The results presented are based on measurements with beams of 136 MeV ^{127}I and 239 MeV ^{197}Au in a 30° recoil geometry. The beams were produced by the Tandem accelerator at the TASCC facility in Chalk River.

II. THEORETICAL CONSIDERATIONS

A. Geometry

The geometry of a typical experimental setup for ERDA is shown in Fig. 1. In the laboratory frame a monoenergetic beam of energy E_0 is incident on a target at an angle α with respect to the surface normal. Target atoms recoiling at an angle ξ are detected with an energy E_2,

$$E_2 = kE_0 = E_0 \frac{4M_1M_2}{(M_1+M_2)^2}\cos^2\xi. \tag{1}$$

M_1 and M_2 are the masses of the incident ion and the target atom, respectively. Recoils appear at angles ξ up to 90°. The energy of the recoil can be approximated to

$$E_2 \simeq \frac{E_0}{M_1} 4M_2\cos^2\xi, \tag{2}$$

[a]Also with Departments of Physics and Astronomy and Engineering Physics, McMaster University, Hamilton, Ontario L8S 4M1, Canada.

 0021-8979/94/76(8)/4524/9/$6.00

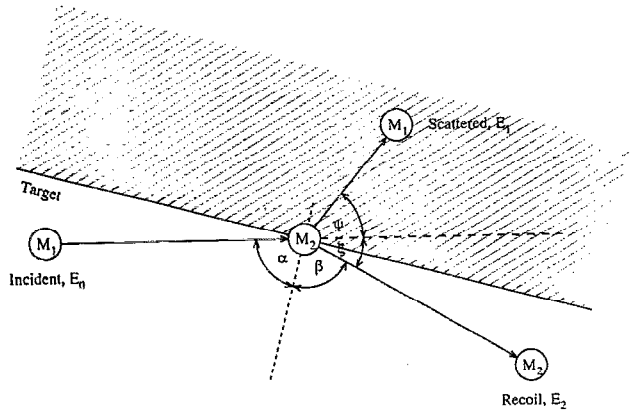

FIG. 1. Schematic showing the scattering geometry of the heavy-ion elastic recoil experiment.

provided the projectile mass M_1 is much heavier than the recoil mass M_2 ($M_1 \gg M_2$). As long as Eq. (2) is valid, the recoil energy is proportional to its mass and to the energy per mass unit E_0/M_1 of the projectile. For a Cl beam, Eq. (2) is a reasonable approximation up to mass 7 (Li), while it is good up to mass 24 (Mg) for an ^{127}I projectile. Hence, for a heavy projectile, the energies of heavy recoils are higher, given a fixed energy per mass unit of the projectile. This makes the detection of heavy elements accessible by the ERDA technique and offers the possibility of profiling a wide range of elements in a single measurement. In the region of validity of Eq. (2), a projectile energy of 1 MeV/u results in recoil energies of 3 and 1 MeV/u for recoil geometries of 30° and 60°, respectively.

Another advantage of heavy projectiles is that only heavy target atoms are able to scatter the projectile beam directly into the detector. Whenever the maximum scattering angle θ_{max} of the projectile is smaller than the detection angle, the observed spectra are much simpler and the count rate as well as the dead time of the detector are greatly reduced. The maximum scattering angle for a given projectile/target combination is

$$\theta_{max} = \sin^{-1}\left(\frac{M_2}{M_1}\right). \tag{3}$$

Target atoms heavier than ^{16}O can scatter a Cl beam into angles larger than 30°, while for a ^{197}Au projectile, only target atoms heavier than mass 100 can do so.

B. Sensitivity

In materials science the sensitivity of an analysis technique is very important, since impurity levels are in the ppm range for most processes in device fabrication. The sensitivity in an ion-beam experiment can be increased by moving the detector closer to the target and thus increasing the solid angle Ω; however, the energy spread, due to the range of recoil angles, limits how much Ω can be increased, without excessive loss in depth resolution.

The sensitivity depends, not only on Ω, but also on the recoil cross section $\sigma(\xi)$. This may be calculated from the scattering cross section in the center-of-mass frame,

$$\sigma_{CM}(\theta) = \left(\frac{e^2}{16\pi\epsilon_0}\right)^2 \left(\frac{Z_1 Z_2}{E_{CM}}\right)^2 \frac{1}{\sin^4(\theta/2)}, \tag{4}$$

and the relation between recoil angle ξ and scattering angle of the projectile θ,

$$\theta = \pi - 2\xi, \tag{5}$$

with the energy in the center-of-mass frame

$$E_{CM} = \frac{M_2}{M_1 + M_2} E_0. \tag{6}$$

Transformation of the recoil cross section to the laboratory frame gives

$$\sigma(\xi) = \left(\frac{e^2}{8\pi\epsilon_0}\right)^2 \left(\frac{Z_1 Z_2 (M_1 + M_2)}{M_2 E_0}\right)^2 \frac{1}{\cos^3 \xi}. \tag{7}$$

For very heavy projectiles ($M_1 \gg M_2$), $M_1 + M_2$ can be approximated to M_1. Hence, the cross sections are roughly proportional to $(Z_1 M_1)^2$. To achieve similar recoil energies, the projectile energy has to be proportional to the projectile mass (i.e., $E_0 \propto M_1$) and the M_1 dependence cancels out. In the case of similar recoil energies the cross section is proportional to Z_1^2, leading to a higher sensitivity of heavy projectiles. Note that for $M_1 \gg M_2$, $\sigma(\xi)$ is almost independent of recoil mass, because for all elements (except H) the ratio between charge and mass is almost constant ($Z_2/M_2 \sim 0.4-0.5$) and $(M_1 + M_2) \sim M_1$. For H recoils, however, the cross section is increased by about a factor of 4, since in this case Z_2/M_2 is unity.

Because of the $\cos^{-3} \xi$ dependence, the cross section increases strongly at larger detection angles. Moving the detector from 30° to 45° or even 60° increases the cross section by a factor of 1.8 and 2.8, respectively; however, this reduces the recoil energy, which means higher projectile energies (leading to smaller cross sections) are necessary in order to obtain recoils of the same energy. This can usually be done, without departing from the Rutherford scattering regime, provided higher energies are achievable; but in most accelerator laboratories, the incident ion energy which is available is the limiting factor.

C. Species resolution

In order to separate different recoils various techniques can be used. Each technique has its advantages and disadvantages, depending on the experimental parameters; e.g., the type and the energy of the projectile. In principle, there are two possibilities to differentiate the recoils: (i) by their mass, and (ii) by their nuclear charge via their rate of energy loss.

The separation by recoil mass can be accomplished via a time-of-flight (TOF) technique. In a TOF setup both the time of flight along a fixed path and the energy are measured for each recoil. The time of flight allows different recoil species with the same energy to be separated. The species resolution of TOF is given by the time difference at the maximum

energy of the recoil species. The difference in time of flight Δt for two elements with mass M_a and M_b is given by

$$\Delta t = 7.1979\times10^{-8} l \frac{\sqrt{M_b}-\sqrt{M_a}}{\sqrt{E_b}}$$

$$= 7.1979\times10^{-8} l \left(\frac{M_b}{E}\right)^{1/2}\left[1-\left(\frac{M_a}{M_b}\right)^{1/2}\right]. \quad (8)$$

With the energy E in MeV, the mass M in u, and the length l in m, the time Δt is in s. Assuming that Eq. (2) is valid and the energy of a recoil is proportional to its mass (E/M_b=const) the mass resolution is given by $1-\sqrt{M_a/M_b}$. For heavy elements $\sqrt{M_a/M_b}$ becomes close to unity for adjacent elements, thus making their separation more difficult compared to light ones.

Using a light projectile has the advantage that the energy of the heavy recoils is no longer proportional to their mass, which means they are easier to separate with TOF. Hence, TOF is well suited for use with light projectiles, while it is not very useful in conjunction with heavy projectiles. Because of the geometry, TOF usually results in very small solid angles (typically ~0.1 msr) which limits the achievable sensitivity.

Another way to separate different recoil species is through their energy loss in a gas counter. A good overview of different gas counters for particle identification is given by Assmann.[18] Gas counters can be divided into two groups, the Bragg counter and various types of ΔE-E counters. Special types of gas counter offer solid angles of up to 7.5 msr.[16]

Gas counters require a thin window that separates the vacuum chamber from the gas volume. This causes a significant energy loss and energy straggling, especially for the heavier recoils. For this reason heavy recoils have to be quite energetic and therefore the use of a gas counter as a detector only makes sense in conjunction with high-energy heavy projectiles.

The species resolution is given by the difference in stopping power for different elements. Figure 2 gives the electronic energy loss for different elements in butane for energies up to 100 MeV. The hatched areas indicate the energies of recoils coming from the surface and from up to 1 μm depth in a Si sample, with a 136 MeV ^{127}I beam with 30° recoil geometry. The figure shows that, for elements up to Ni, the difference in stopping power is sufficient to allow their separation over a depth of 1 μm. Hence, a ΔE-E detector is a good choice for simultaneous particle identification over a very wide range of Z_2.

D. Experimental limitations

When using ERDA as an analysis technique, some additional complications have to be considered. One of these is the sputtering process. Following Feldman and Mayer (Ref. 19, pp. 79–80), the sputtering yield Y may be estimated from the nuclear stopping power $dE/dx|_n$ and the surface binding energy U,

$$Y = \alpha \frac{0.042}{NU}\left.\frac{dE}{dx}\right|_n, \quad (9)$$

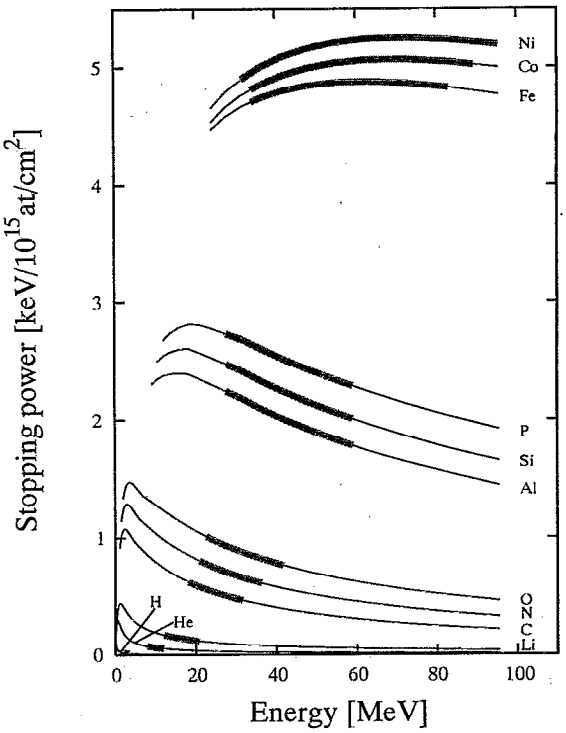

FIG. 2. Electronic energy loss of different elements in isobutane. In addition, the surface recoil energies of the elements for our specific experimental conditions (136 MeV I and 30° recoil angle) are shown.

where α is a function of the mass ratio M_2/M_1 and the angle of incidence. For 136 MeV I on Si at 15° to the surface, α=0.8 and U=3 eV/atom. Substitution in Eq. (9) gives a sputtering yield $Y\sim0.5$ Si atoms per incident ion. Hence, a bombardment dose of $\sim2\times10^{13}$ ions/mm^2 would be required to sputter away 1 monolayer. Since our typical heavy-ion ERDA (HIERDA) bombardment (Figs. 4–11) involves only 1×10^{12} iodine atoms/mm^2, sputtering effects are normally not a problem.

However, in some molecular targets (e.g., Si_3N_4), electronic energy loss sometimes produces volatile products such as N_2, due to the breaking of chemical bonds. This electronic sputtering can be up to 1–2 orders of magnitude larger than the above sputtering estimate of 0.5 atoms/ion.[20]

As mentioned above, ERDA analysis is very simple as long as the recoil cross sections are all Rutherford. In a scattering event, the closest approach of the two atoms is given by

$$D = \frac{Z_1 Z_2 e^2}{2E}\frac{M_1+M_2}{M_2}\left(1+\frac{1}{\cos\xi}\right). \quad (10)$$

For Rutherford scattering, the closest approach should not be smaller than 3–4 times the sum of the nuclear radii.[21] Using Eq. (10), the calculations show that the recoil cross sections are Rutherford throughout the projectile energy regime of 0.5–2.0 MeV/u.

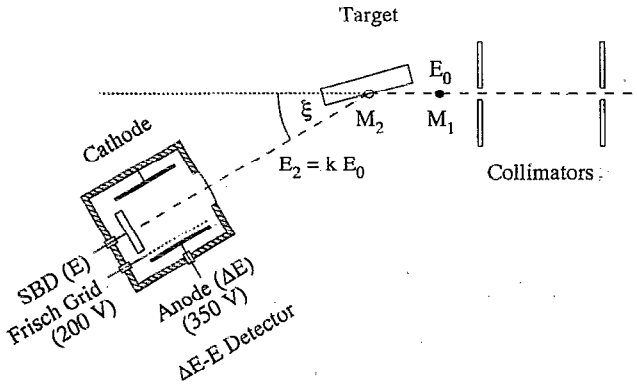

FIG. 3. Schematic showing the experimental setup and the ΔE-E detector.

E. Depth resolution

In addition to the sensitivity, the depth resolution is also a very important parameter, especially if layered structures are studied, where the change of an impurity concentration at the interface is needed. The depth resolution is given by the energy losses ϵ_P and ϵ_R of the ingoing projectile and the recoil atom, respectively. It is limited by the energy spread of the detected particle $\delta E_{\delta\xi}$, due to a change of the recoil angle over the detector, and the energy straggling in the detector window δE_W and in the target; δE_{SP}, δE_{SR} are the energy straggling of the ingoing projectile and outgoing recoil, respectively. The depth resolution is then given by

$$\frac{\sqrt{\delta E_{\delta\xi}^2+(k\,\delta E_{\mathrm{SP}})^2+\delta E_{\mathrm{SR}}^2+\delta E_W^2}}{(k\epsilon_P/\cos\alpha)+(\epsilon_R/\cos\beta)}. \tag{11}$$

The higher value of ϵ_P for heavy projectiles is almost fully compensated by their smaller k values and therefore does not result in a better depth resolution; however, for heavy projectiles the energy spread $\Delta E_{\delta\xi}$ for a similar change in recoil angle is larger compared to light projectiles. Hence, the solid angle has to be decreased in order to maintain the same depth resolution. This can be accomplished without any loss in sensitivity, because of the higher cross sections. The use of a detector as described by Assman *et al.*[16] enables one to utilize fully the higher sensitivity arising from the large heavy-ion σ values, without losses in terms of depth resolution.

F. Summary

The considerations of this section show: (i) a heavy projectile allows the simultaneous profiling of a wider mass range of recoils (all masses $\lesssim M_1/2$), because of the better energy transfer for a heavier projectile; (ii) since the mass resolution of TOF breaks down in the energy and mass region accessible with heavy projectiles, a ΔE-E detector is the best choice for particle identification. A ΔE-E detector also provides a larger solid angle than TOF.

III. EXPERIMENTAL TECHNIQUE

The recoils were detected in a specially designed ΔE-E detector (Fig. 3). Compared to the Bragg detector used in our previous studies,[20] the ΔE-E detector has a very simple design. The ΔE part of the detector is a gas detector, consisting of a pair of plates 4 cm long and located directly behind the entrance window. The residual energy of the particles after traveling through this ΔE detector is measured in a surface barrier detector (SBD), mounted inside the gas chamber (Fig. 3). Use of an SBD enables the residual energy to be measured with very good resolution.

This gas counter/SBD detector assembly is mounted via a 2 in. flange to the scattering chamber. A valve between the target chamber and the detector allows venting of the target chamber, while the detector is kept under operating pressure. We chose mounting flanges for the detector at recoil geometries of 60° and 30°, thus enabling us to take advantage either of the higher cross sections at 60° or of the enhanced depth resolution and higher recoil energies at 30°. Because of the distance between target and detector, our solid angle is relatively small (0.73 msr).

Isobutane at pressures between 20 and 80 Torr was used as the detector gas. Higher gas pressures allow the detection of low-Z elements such as H and He in the coincidence spectrum. The anode was biased to +350 V, while the Frisch grid was at +200 V and the cathode at ground potential. The low gas pressure allows the use of very thin entrance windows. In our initial test, a 250 μg/cm^2 thick Mylar window was used, but thinner windows are available. The results shown here are all for a scattering geometry of 30° with either 136 MeV I or 239 MeV Au beams.

A. Energy calibration

To extract depth profiles from the recoil spectra, an energy calibration of the detector is necessary. In principle there are two ways to calculate the ΔE-E detector.

One way is to calibrate both the gas counter (ΔE detector) and the SBD (E detector). This involves a calibration with various ions, in order to account for the pulse height defect, due to high plasma densities in the gas counter. In addition, the energy loss of different ions in the detector window has to be determined, preferably at various energies.

Since this would be a very time consuming procedure, we chose a more empirical approach. A particle with energy E_2 loses energy in the window $[\Delta E_W(E_2,R)]$ and in the detector gas $[\Delta E_G(E_2-\Delta E_W,R)]$, before it hits the SBD. The energy loss is a function of the recoil species R and the energy. Over a wide range of energies the energy loss in the gas detector changes quite slowly with energy (see Figs. 4, 5, 7–9, and 11). This can be seen from the almost linear slope of the curves for each element in the ΔE-E coincidence spectra. For elements up to P, the energy loss in the gas counter decreases slowly with increasing energy, while it is almost constant for Ga and As. For still heavier recoils such as In, there is a slow linear increase.

For much lower energies, the energy loss in the detector gas deviates from linear behavior, but at these energies the curves of different elements merge into each other and they cannot be analyzed anyway. The residual energy E_D of a particle hitting the SBD (E detector) can be written as

$$E_D=E_2-\Delta E_W(E_2,R)-\Delta E_G(E_2-\Delta E_W,R). \tag{12}$$

This equation gives the relation between the SBD signal and the recoil energy E_2. It can be determined by measuring the pulse height of the surface recoils at various projectile energies. In a first approximation, this relation is linear, thus leading to

$$E_2 = E_{\text{off}} + \Delta E_{\text{chn}} N_{\text{chn}}, \tag{13}$$

where E_{off} is the sum of the energy loss in the gas and the window. If ΔE_W and ΔE_G do not change over the energy range of the calibration, ΔE_{chn} is simply the pulse-height–to–energy conversion of the SBD detector. If they change, ΔE_{chn} also includes the change of the energy loss. In fact, for light elements (up to Si) ΔE_{chn} is somewhat smaller than the value derived for an α-particle source, while it is larger for In.

An energy calibration has to be done for each recoil species, but several species can be calibrated simultaneously. This calibration can be done rather quickly and avoids all complications such as pulse height defect, etc., since it provides directly an empirical relation between the pulse height of SBD signal and the recoil energy. Since this relation is linear over the useful energy range, three or four different projectile energies are sufficient to provide a good calibration.

B. Calculation of the composition profile

This subsection describes the procedure used to convert a spectrum into a composition profile. In general, HIERDA allows the simultaneous measurement of all components of a sample. Hence, the energy spectra can be directly converted to a concentration profile. As an experimental parameter only the energy calibration for each element is necessary. The solid angle Ω and the fluence are not needed in the calculation, which eliminates an additional source of error.

A HIERDA experiment usually has a wide variety of ion/target combinations. In order to accommodate this fact in a computer program, a data set is needed that contains all possible ion/target combinations. This is the case for the TRIM stopping power tables; therefore the TRIM tables were used.[22] The energy loss of composite targets is calculated according to Bragg's rule. Cross sections are calculated from Eq. (7), with the screening corrections given by Andersen *et al.*[23]

The recoil yield Y_i of a target element i is given by

$$Y_i = N\Omega \Delta E_i \frac{\sigma_i(E)}{\epsilon_i} c_i, \tag{14}$$

where N is the number of projectile atoms, Ω the detector angle, ΔE_i the energy width per channel, σ_i the cross section, and c_i the concentration. ϵ_i is the sum of the energy loss of projectile and recoil in the target and is given by

$$\epsilon_i = k_i \sum_j c_j \epsilon_{pj}(E) + \sum_j c_j \epsilon_{ij}(k_i E), \tag{15}$$

where E is the projectile energy.

The sum of all target components has to add up to unity and therefore the concentration of each component is given by

$$c_i = \frac{Y_i \epsilon_i}{\Delta E_i \sigma_i} \frac{1}{N\Omega}, \tag{16}$$

with

$$\sum_i c_i = 1 \Rightarrow N\Omega = \sum_i \frac{Y_i \epsilon_i}{\Delta E_i \sigma_i}. \tag{17}$$

An iterative procedure has to be used to calculate c_i from Y_i, since the concentrations of the elements also determine ϵ_i.

In the first step, the energy of the surface recoils for each component is calculated. With the energy calibration for the species, the surface yield is taken from the spectra and the surface concentrations are calculated from Eqs. (16) and (17), as described above. Then the energy loss in a layer with a thickness Δd is calculated, with the surface concentrations determined in the first step. This leads to the recoil energies from this depth. Again, the yields are determined from the spectrum and converted into concentrations. With these concentrations the energy of the recoil originating from one step deeper in the sample is calculated. In this way the calculation proceeds through the sample.

In determining the distribution at a certain depth, the distribution at shallower depths has to be known in order to calculate the energy loss. Since the calculation starts at the surface, this requirement is always fulfilled.

The value of $N\Omega$ has to remain constant over the whole profiling depth, since the number of incoming projectiles and the solid angle is constant; therefore, $N\Omega$ provides a test on the consistency of the calculation. Variations in $N\Omega$ indicate either that an error has been made in the energy calibration or that a substantial target component is missing.

IV. RESULTS AND DISCUSSION

Various samples have been measured in order to demonstrate the species and depth resolution as well as the sensitivity of the technique.

Figure 4 shows the ΔE-E coincidence spectrum of a stainless-steel sample taken with a 136 MeV ^{127}I beam and a gas pressure of 20 Torr in the ΔE detector. The x axis gives the pulse height in the surface barrier detector (E detector), while the y axis gives the pulse height observed in the ΔE detector. The density of the dots is proportional to the number of counts. The (roughly horizontal) bands seen in the figure correspond to the different elements present in the stainless-steel sample. Beginning at low ΔE, the following elements can be identified: carbon, nitrogen (in very small amounts), oxygen (mostly at the surface, i.e., around channel 100), silicon; and the principal components of stainless steel: chromium, iron, and nickel. The spectrum demonstrates nicely the separation of Cr, Fe, and Ni. Using a higher gas pressure of 40 Torr increases the separation even more and enables the separation of adjacent elements up to Ni.

From the spectrum the composition of the steel was calculated to be 75% Fe, 9% Ni, and 15% Cr. Si and C are present in a concentration of 0.8% and 0.3%, respectively. The N and O concentration are below 0.2% and 0.1%, re-

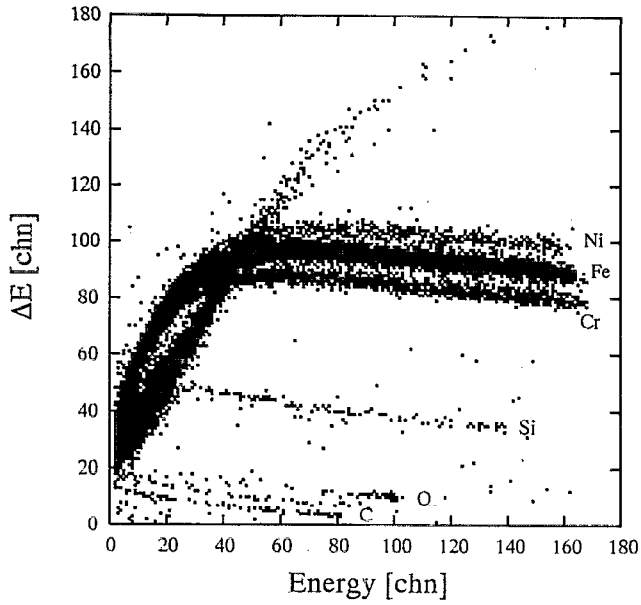

FIG. 4. Coincidence spectrum of stainless steel taken with 136 MeV ^{127}I beam and a gas pressure of 20 Torr in the ΔE detector.

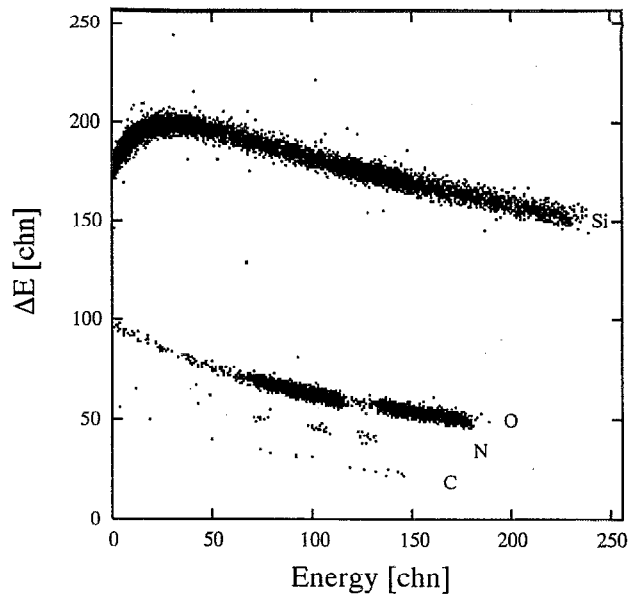

FIG. 5. Coincidence spectrum of a SIMOX sample, taken with a 136 MeV ^{127}I beam and a gas pressure of 40 Torr in the ΔE detector.

spectively. Between Si and Cr are a few data points which can be related to K or Ca, but the concentration is less than 0.01%.

The other feature visible in the spectrum is an intense band at low E, which intercepts with the major lines from Cr, Fe, and Ni around channel 40. This is due to iodine projectiles undergoing plural scattering events in the target. Note that 27° is the maximum scattering angle of ^{127}I on Fe or Ni. Hence, it requires at least two scattering events for iodine to reach the detector; however, iodine scattered by ~15° could travel almost parallel to the surface and hence has a high probability of undergoing another scattering event to the detector.

Figure 5 gives the spectrum of a Si sample with a buried and a surface SiO_2 layer. In this separation by implantation of oxygen (SIMOX) sample Si, O, and traces of N and C are clearly identified. The N is concentrated at three well-resolved depths. Figure 6 gives the concentration profile of the components Si, O, and N as a function of depth, calculated with the computer program described above. Four distinct layers are clearly resolved: surface SiO_2, Si, buried SiO_2 and bulk Si. Their thicknesses are 330 and 290 nm for the top and buried SiO_2 layers, respectively, and 200 nm for the intervening Si layer. These values are in good agreement with electron microscopy results of 350 and 290 nm for the SiO_2 layers and 180 nm for the Si layer between.

The depth profiles in Fig. 6 show that the nitrogen is accumulated at the three Si/SiO_2 interfaces. The amount of N at each interface is $5-10\times10^{15}$ atoms/cm^2, while the total amount of C in the sample is around $5-10\times10^{15}$ atoms/cm^2.

Figure 7 shows a multilayered sample of alternating layers of InP and $In_xGa_{1-x}As$ ($x=0.54$) on bulk InP. The sample consists of three InP layers (40, 80, and 150 nm) and three $In_xGa_{1-x}As$ layers (60, 120, and 180 nm). The graph shows that in the P-recoil spectrum all six layers are resolvable, while in the case of Ga and As recoils only the top five layers are resolvable. The Ga and As recoils which come from the deepest InGaAs layer merge with the signal which stems from scattering iodine projectiles. This gives a probing depth of about 300–400 nm for Ga or As and 700–800 nm for Si and P under these conditions. The lower-Z elements are well separated over their whole probing depth, but Ga and As are only separated within the uppermost 150 nm.

The very intense line, which does not bend over at higher energies, is due to a mixture of In recoils and scattered I projectiles. Since iodine can be scattered by In into angles greater than 30°, scattered iodine is detected as well. Scattered projectiles in the detector could be minimized by going to larger detection angles and/or using heavier projectiles, such as ^{197}Au.

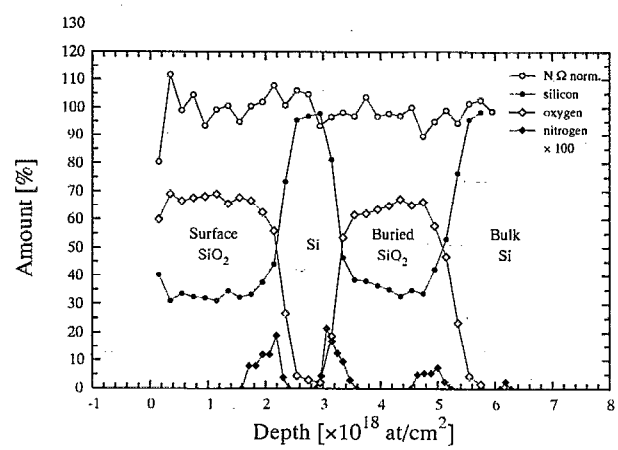

FIG. 6. Depth profiles of the elements in a SIMOX sample, calculated from the spectrum in Fig. 5. Four clearly resolvable regions are: (1) surface SiO_2 (330 nm); (2) Si (200 nm); (3) buried SiO_2 (290 nm); (4) bulk Si.

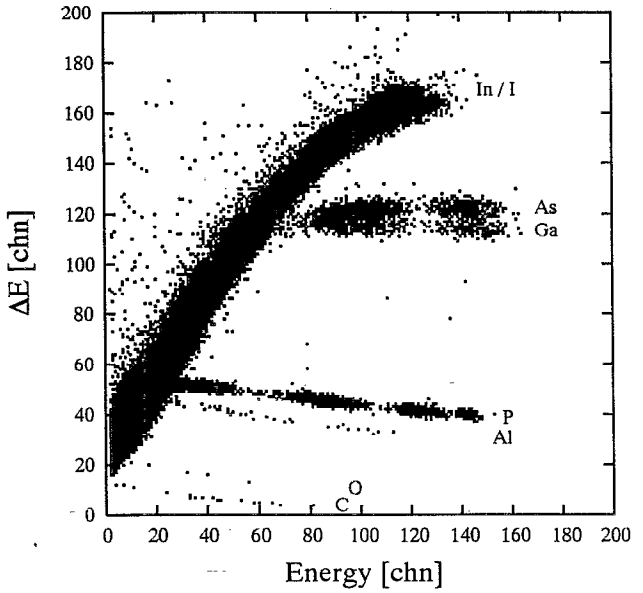

FIG. 7. Coincidence spectrum of an indium phosphide sample with three alternating layers of InP and $In_xGa_{1-x}As$ ($x=0.54$). The spectrum was taken with a 136 MeV ^{127}I beam and a gas pressure of 20 Torr in the ΔE detector.

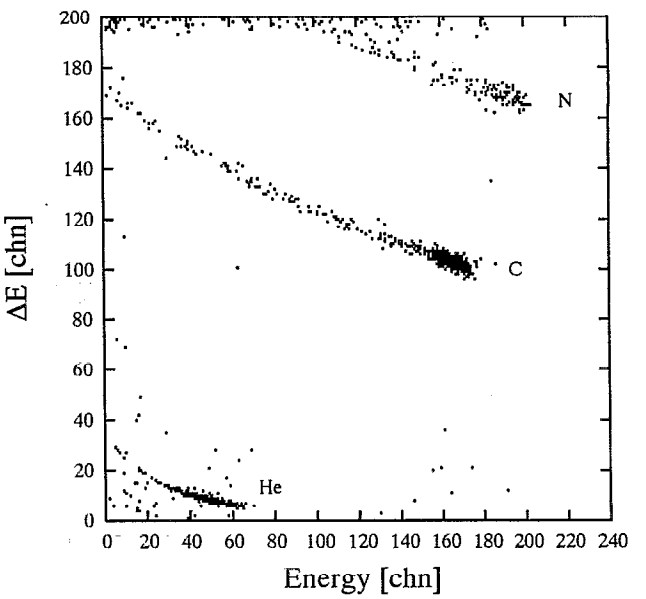

FIG. 9. Coincidence spectrum of a Si sample implanted with 2×10^{17} He/cm^2. The spectrum was taken with a 136 MeV ^{127}I beam and a gas pressure of 80 Torr in the ΔE detector.

Figure 8 shows the coincidence spectrum of the same sample taken with a 239 MeV Au beam and a gas pressure of 60 Torr in the ΔE detector. Au can still scatter on In into angles greater than 30°, but compared with the iodine beam (Fig. 7) the energy loss of Au varies significantly from the energy loss of In and both signals can now be resolved. A change in intensity in the In line can be seen and is due to the varying In concentration in the layers. The probing depth in this case is much larger, i.e., around 700–800 nm for Ga and As and about 1500 nm for P, due to the higher-energy transfer. Hence, all three GaAs layers are now visible.

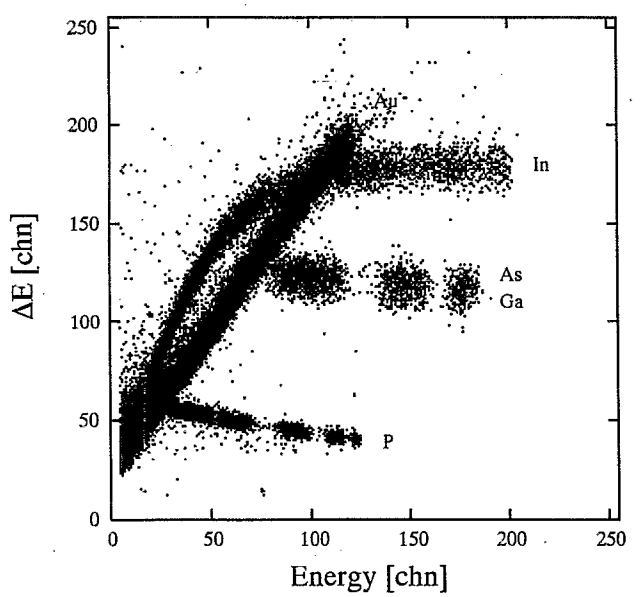

FIG. 8. Coincidence spectrum of an indium phosphide sample with three alternating layers of InP and $In_xGa_{1-x}As$ ($x=0.54$). The spectrum was taken with a 239 MeV Au beam and a gas pressure of 60 Torr in the ΔE detector.

Figure 9 shows the coincidence spectrum of a Si sample that had been preimplanted with He. The spectrum is taken at a higher gas pressure of 80 Torr. Due to the higher gas pressure, He loses enough energy in the ΔE detector to produce a signal that is well above the noise level. The signal height of elements heavier than N is now above the dynamic range of the amplifier, since they lose too much energy in the ΔE detector at 80 Torr. Therefore, the coincidence spectrum shows only events resulting from He, C, and N recoils. A coincidence spectrum taken at a gas pressure of 40 Torr reveals the buildup of surface contamination (C, N, and O) during the He preimplantation, while the spectrum taken at higher gas pressure shows the profile of the implanted He. Going to a still higher gas pressure (120 Torr) enabled us to detect even H in the ΔE detector.

In order to obtain coincidence spectra from both the light and heavy elements, two runs at different gas pressures are necessary. This is not very practical. Therefore, at the lower gas pressure (40 Torr), we in addition recorded those events in the solid-state detector, which are above the noise level but are not in coincidence with any ΔE signal. This noncoincidence energy spectrum is due to low-Z recoils, which have a below-threshold ΔE signal. At 40 Torr gas pressure this is the case for H, He, and Li recoils at high energies.

The noncoincidence energy spectrum from the He-implanted sample is shown in Fig. 10. This spectrum was taken simultaneously with a coincidence spectrum at a gas pressure at 40 Torr. The spectrum shows two peaks: one at ~11 MeV and the other at ~3 MeV. These two peaks are due to the implanted He and to H incorporated in the surface contamination. This demonstrates that all elements from H

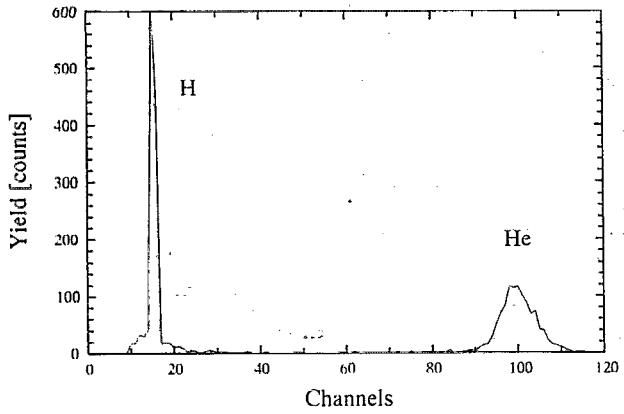

FIG. 10. H and He recoil spectrum of a Si sample implanted with 2×10^{17} He/cm^2. The spectrum shows the noncoincident events in the surface barrier detector. The H is an impurity introduced during the He implantation.

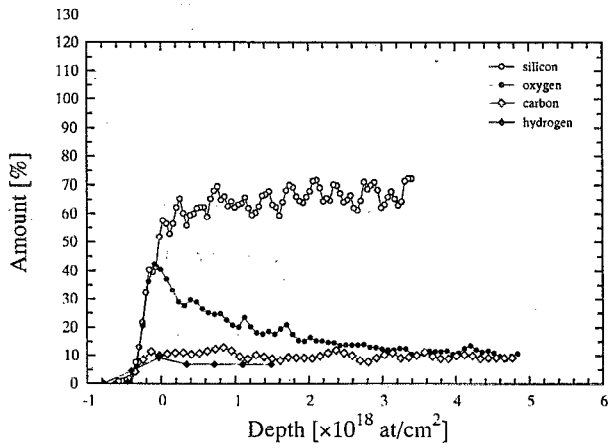

FIG. 12. Composition profile of porous silicon. The profile is calculated from the spectrum shown in Fig. 11.

up to Si and even higher can be profiled within a single measurement.

Figure 11 shows the coincidence spectrum of a porous silicon sample, taken with a 136 MeV ^{127}I beam and a gas pressure of 40 Torr. The spectrum shows the presence of large amounts of C and O as well the major component of Si. From the noncoincidence spectrum hydrogen was identified as another major component. There are also detectable amounts of F, Cl, and N present. The F originates from the HF etch, in which the porous silicon was produced. During the HF etch the back electrode of the silicon sample was protected by wax, which was subsequently removed using trichlorethane. The Cl in the sample is presumably introduced by this cleaning procedure, since Cl is only present in samples on which the wax had been removed.

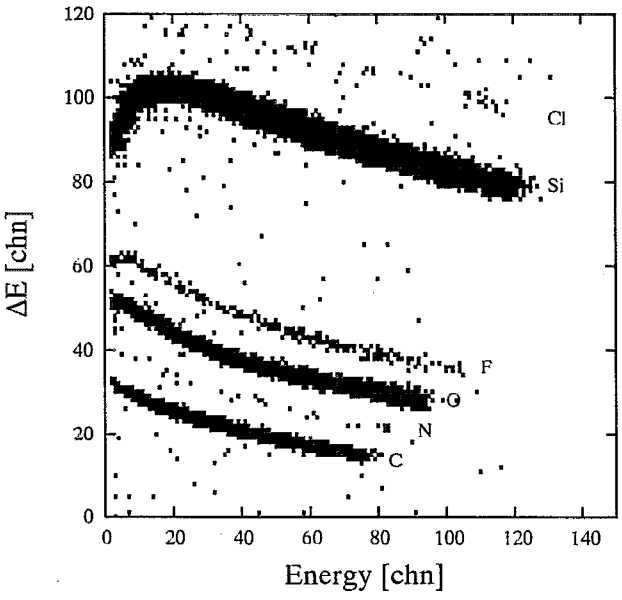

FIG. 11. Coincidence spectrum of a porous silicon sample, taken with a 136 MeV ^{127}I beam and a gas pressure of 40 Torr in the ΔE detector. The spectrum shows not only the major components of porous silicon, C, O, and Si, but also traces of N, F, and Cl.

From the energy spectra of all the elements present in the sample the composition profile was calculated and the result of the calculation is shown in Fig. 12. N, F, and Cl are not plotted in the figure, since they are only present in trace amounts.

The figure shows a constant C concentration (~10%) over the whole depth, while the O concentration peaks at the surface (~40%) and then falls gradually toward its 10% level. This may be due to an oxide layer present prior to the anodic etching of the sample. The H content is fairly constant at ~10%.

V. CONCLUSIONS

We have shown that ERDA with heavy ions is very well suited for solving problems in device fabrication and materials science. With ^{127}I projectiles, a sensitivity of 10^{15} at./cm^2 or better is achievable. In a 1 μm layer this is equivalent to 50–100 ppm. Separation of adjacent elements up to Si and P is readily accomplished. Heavy ions also allow the profiling of elements up to In, with almost elemental resolution up to Ga and As. All elements from H up to the heaviest components can be measured simultaneously. A depth resolution down to 20–30 nm can be achieved.

ACKNOWLEDGMENTS

We gratefully acknowledge the excellent technical assistance of J. A. Cave in building the ΔE-E detector, as well as the technical assistance of J. J. Hill and P. J. Jones with the TASCC beamline facilities. We also thank I. Emesh and T. MacElwee for the SIMOX samples and B. J. Robinson for the InP/InGaAs sample. H.K.H. and J.A.D. thank the Natural Sciences and Engineering Research Council (NSERC) of Canada for their financial support.

[1] *Ion Beam Handbook for Material Analysis*, edited by J. W. Mayer and E. Rimini (Academic, New York, 1977).
[2] J. A. Davies, F. J. D. Almeida, J. S. Forster, H. K. Haugen, T. E. Jackman, and R. Siegele, Nucl. Instrum. Methods B **85**, 28 (1994).

[3] J. L'Ecuyer, C. Brassard, C. Cardinal, J. Chabbal, L. Deschênes, J. P. Labrie, B. Terreault, J. G. Martel, and R. St.-Jacques, J. Appl. Phys. **46**, 381 (1976).
[4] J. L'Ecuyer, C. Brassard, C. Cardinal, and B. Terreault, Nucl. Instrum. Methods **149**, 271 (1978).
[5] B. L. Doyle and P. S. Peercy, Appl. Phys. Lett. **34**, 811 (1979).
[6] R. Groleau, S. C. Gujarthi, and J. P. Martin, Nucl. Instrum. Methods **218**, 11 (1983).
[7] J. P. Thomas, M. Fallavier, D. Ramdane, N. Chevarier, and A. Chevarier, Nucl. Instrum. Methods **218**, 125 (1983).
[8] M. Petrascu, I. Berceanu, I. Brancus, A. Buta, M. Duma, C. Grama, I. Lazar, I. Mihai, M. Petrovici, V. Simon, M. Mihaila, and I. Ghita, Nucl. Instrum. Methods B **4**, 396 (1984).
[9] J. P. Thomas, M. Fallavier, and A. Ziani, Nucl. Instrum. Methods B **15**, 443 (1986).
[10] H. J. Whitlow, G. Possnert, and C. S. Petersson, Nucl. Instrum. Methods B **27**, 448 (1987).
[11] A. M. Behrooz, R. L. Headrick, L. E. Seiberling, and R. W. Zurmühle, Nucl. Instrum. Methods B **28**, 108 (1987).
[12] E. Hentschel, R. Kotte, H. G. Ortlepp, F. Stray, and D. Wohlfarth, Nucl. Instrum. Methods B **43**, 82 (1989).
[13] J. P. Stroquert, G. Guillaume, M. Hage-Ali, J. J. Grob, C. Ganter, and P. Siffert, Nucl. Instrum. Method B **44**, 184 (1989).
[14] B. Gebauer, D. Fink, P. Goppelt, M. Wilpert, and Th. Wilpert, Nucl. Instrum. Methods B **50**, 159 (1990).
[15] R. Behrisch, R. Grötschel, E. Hentschel, and W. Assmann, Nucl. Instrum. Methods B **68**, 245 (1992).
[16] W. Assmann, P. Hartung, H. Huber, P. Staat, H. Steffens, and Ch. Steinhausen, Nucl. Instrum. Methods B **85**, 726 (1994).
[17] W. Assmann, H. Huber, Ch. Steinhausen, M. Dobler, H. Glückler, and A. Weidinger, Nucl. Instrum. Methods B **89**, 131 (1994).
[18] W. Assmann, Nucl. Instrum. Methods B **64**, 267 (1992).
[19] L. C. Feldman and J. W. Mayer, *Fundamentals of Surface and Thin Film Analysis* (North-Holland, New York, 1986).
[20] R. Siegele, J. A. Davies, J. S. Forster, and H. R. Andrews, Nucl. Instrum. Methods B **30**, 606 (1994).
[21] J. Räisänen, E. Rauhala, J. M. Knox, and J. F. Harmon, J. Appl. Phys. **75**, 3273 (1994).
[22] J. F. Ziegler, J. P. Biersack, and U. Littmark, *The Stopping and Range of Ions in Solids* (Pergamon, New York, 1985).
[23] H. H. Andersen, F. Basenbacher, P. Loftager, and W. Möller, Phys. Rev. A **21**, 1891 (1980).